Development of a Digital Rock Physics workflow for the analysis of sandstones and tight rocks

I. Verri [a], A. Della Torre [a,*], G. Montenegro [a], A. Onorati [a], S. Duca [b], C.A. Mora [b], F. Radaelli [b], G. Trombin [b]

[a] *Politecnico di Milano, Department of Energy, Via Lambruschini 4, 20156, Milano, Italy*
[b] *Eni S.p.A., Via Emilia 1, 20097, San Donato Milanese, Milano, Italy*

Predicting petrophysical properties by means of digital core analysis strongly relies on the operator expertise and becomes very challenging when dealing with clay microporosity, due to resolution limits and a general lack of recommendations. In the standard workflow, 3D images of rock samples are acquired via X-ray computed to-mography and processed, to reconstruct pore geometries that are used to set up numerical experiments for the calculation of physical properties, such as permeability. In the present paper, the limits of the standard workflow are investigated and specific strategies are proposed to make the entire process less operator dependent and more reliable when dealing with tight samples. A global thresholding technique is applied for the identification of the pore space. The quality of its performance has been found to be strongly related to contrast, noise and presence of rock microporosity. Threshold selection is more robust if contrast enhancement and denoising algorithms, like bilateral filter and non-local means, are applied. Furthermore, microporosity shall not be excluded from the reconstructed pore space, since it is fundamental in providing connectivity of the flow paths. The selected value for thresholding is used inside an image-based meshing strategy, to create a computational grid directly on the 3D stack of images. Methods to compute porosity, specific surface and average pore diameter are described. Absolute permeability is computed by performing Computational Fluid Dynamics (CFD) simulations of single-phase incompressible flows in the reconstructed pore space. A model to include the presence of an increased resis-tance to the fluid flow in the microporous region is proposed and validated by comparison with experimental measurements.

1. Introduction

Along with conventional reservoirs, low-permeability formations are nowadays considered as valuable resources for oil and gas production (U.S. Energy Information Administration, 2015; American Association of Petroleum Geologists, 2015). The economic assessment prior to field development cannot avoid an accurate evaluation of rock properties, such as porosity, permeability and capillary pressure. Nonetheless, tight reservoirs are characterized by such low permeabilities, typically less than 0.1 md, that most of the standard techniques applied to assess conventional reservoirs are unpractical and/or lead to unreliable evaluations (Wang et al., 2015).

The limits of traditional experimental methods has rapidly turned digital core analysis into a commercial predictive tool (Blunt et al., 2013;

Fredrich et al., 2014). As a matter of fact, digital analysis is nowadays regarded with interest not only for its capability of predicting the main petrophysical properties, but also because it gives a valuable physical insight into the micro-scale phenomenona. In the standard workflow, cores are imaged, for instance by X-ray micro-tomography, to obtain a digital reconstruction of the inner pore structure. Then, numerical methods are used to simulate single and multiphase flow to retrieve the petrophysical properties of interest. The complete digital process in-volves several modeling choices, such as the choice of the parameters employed for the processing and segmentation of the image, the size of the subvolume used for the simulations, the solver and the boundary conditions. The choice of the representative sample size is particularly critical because it directly affects the computational cost of the numerical simulation (Blunt et al., 2013. Andrä et al., 2013a). Even so, most

* Corresponding author.
  E-*mail address:* augusto.dellatorre@polimi.it (A. Della Torre).

challenges are related to the processing of the image dataset for the reconstruction of the void space, as it is difficult to define a standard workflow able to provide accurate results over wide range of porosities and permeabilities. After the tomographic acquisition images are usually processed, for example by adjusting contrast or by reducing brightness inhomogeneities and noise. At the present, several techniques have been proposed to perform an automatic image editing and segmentation (Schlüter et al., 2014; Iassonov et al., 2009; Eibenberger et al., 2008; Buades et al., 2005; Huang and Chau, 2008), but porosity estimations are still inaccurate in rocks where a significant fraction of the porosity is below the image resolution (Awang et al., 2015; Long et al., 2013; Golab et al., 2010; Sok et al., 2009). As for tight sandstones and carbonates, the resolution of Micro Computed Tomography (micro-CT) scanners, which is in the order of few microns, is not enough to resolve micro-porous structures. On the contrary, these features can be clearly observed and identified with a resolution of nanometers, e.g. with 2D acquisition by means of Scanning Electron Microscope (SEM) or 3D imaging by means of Focused Ion Beam Scanning Electron Microscope (FIB-SEM) (Long et al., 2013; Golab et al., 2010; Sok et al., 2009). Nano resolution images cannot be directly used to construct a computational grid and to perform numerical simulations, due to the limitations in computational resources and to the requirements on the representativeness of the sample. The integration between SEM data and micro-tomography by mapping sub-resolution porosity visible in a 2D SEM image to gray scale levels in a 3D tomographic image has found to be a successful strategy (Sok et al., 2009), but it is still a quite challenging task to be performed, since it requires unconventional experimental procedures for data registration. As a matter of fact, the conventional workflow for image processing is applied also to rocks with a high amount of micro-porosity. Manual thresholding is usually performed targeting a compromise between the need of an accurate representation of the geometry and the loss of detail caused by the low resolution of the images. As a results, rock characterization is subject to a high degree of uncertainty; in particular, comparative studies have shown that the values predicted for porosity and permeability have a variation range with respect to mid-range values that is up to about 30% for porosity and 40% for permeability (Andrä et al., 2013a,b).

In the present study, a complete Digital Rock Physics (DRP) workflow is applied both to conventional and low permeable rock samples following a direct simulation approach. The proposed methodology is implemented on the basis of open-source tools, namely Fiji (Schindelin et al., 2012) and OpenCV (Bradski et al., 2000) for image processing and OpenFOAM® (Weller et al., 1998; OpenFOAM Foundation) for Computational Fluid Dynamics (CFD) simulations. Current challenges in the application of the workflow to tight samples are addressed, aiming at the development of a procedure that is highly automatic and able to improve the reliability in the geometrical and fluid-dynamic characterization of low permeable rocks. The effect of the presence of microporosity on the quality of the segmentation when applying an automatic thresholding is investigated. An image-based mesh generation strategy is developed to minimize the possible loss of accuracy during the reconstruction of the geometry and retain as much information as possible. Moreover, strategies to account for the effect of microporosity on the fluid flow in the numerical simulations are proposed and discussed.

The article is organized as follows. Firstly, the methodology that has been adopted is presented and details for each step are provided. Then, the available datasets of conventional and tight rocks are described. Finally, results for the geometrical and fluid-dynamic properties of the samples are shown and discussed.

2. Methodology

The analyzed Digital Rock Physics (DRP) workflow consists of: (i) image processing, to identify and separate matrix and pores; (ii) the generation of a computational mesh; (iii) performing numerical simulation, to determine the effective properties of the sample.

2.1. Image processing

The image processing phase consists of: (1) cropping; (2) histogram equalization; (3) denoising; (4) segmentation.

Firstly, images are cropped to ensure that edge artifacts at the corners are removed and to allow the choice of a proper Representative Elementary Volume (REV). The histogram equalization technique is used for contrast enhancement. Datasets that are characterized by low contrast show a steep curve for the cumulative density function of gray values, since most of the voxels are concentrated in a narrow range of intensities. Histogram equalization spreads the intensity distribution across the full intensity range (0–255 in a 8-bit image). Due to image integrity reasons, the output image has a nearly flat histogram, with a greater amount of details that are visually distinguishable. Despite contrast enhancement destroys some structural information of the input image (Schlüter et al., 2014), it is necessary to improve the quality of the segmentation, especially if global thresholding is applied (Iassonov et al., 2009). Moreover, contrast enhancement has the practical advantage of making the segmentation algorithm more robust and improving the threshold detection at the same time (Schlüter et al., 2014). The algorithm for histogram equalization has been implemented on the basis of the procedure described in Easwaran (2009) and applied to the full 3D stack at once.

The third step, denoising, is required to improve the signal to noise ratio of tomographic images. Denoising techniques basically apply an averaging between pixels to reduce noise. As a side effect, averaging reduces image detail, typically blurring edge regions or removing small features. In order to avoid excessive loss of details while still improving the reliability of the segmentation, edge-preserving noise reduction filters have been designed (Eibenberger et al., 2008). Among these, there are Bilateral Filter (BF) and Non-Local Means (NLM). The main difference between the two is that in BF averaging is performed over the pixels that surround a target pixel, while in NLM all pixels in the image are considered. For this reason, NLM is expected to be more robust than BF when dealing with noisy data (Buades et al., 2005). NLM is also very efficient in artifacts removal, as for ring effect (Schlüter et al., 2014). In both algorithms, information about pixel location and intensity is stored and used to determine the relative weight within the averaging process. Usually, some input parameters control the averaging window size and intensity limits, but these have to be manually set. BF and NLM versions included in Fiji and OpenCV have been tested. In particular, 2D and 3D implementations are available, except for BF in OpenCV. In this case, its 3D version has been obtained by averaging the output of three sequential 2D slice-by-slice denoising operation performed along the three main directions. Denoising parameters have been varied systematically to study how segmentation and effective properties are affected by different operator choices.

The last step of image processing is segmentation, which aims at identifying the pore space. A histogram-based global thresholding technique has been selected for application, because of its simplicity and its possible extension to multi-region segmentation. Moreover, denoised images of the given samples do not show any significant artifact, so locally adaptive thresholding seem not to be necessary. The threshold value for the pores has been chosen at the first minimum of the stack histogram. This approach avoids any pre-classification of voxels or any assumption about background-foreground classes. For comparison purposes, a more refined strategy based on Gaussian Mixture Models (GMM) has been adopted (Huang and Chau, 2008). The stack histogram is fitted with Gaussian distributions, whose parameters are estimated by the Expectation Maximization (EM) algorithm (Dempster et al., 1977; McLachlan and Krishnan, 2007). The number of Gaussians and initial guesses for the parameters are automatically retrieved by the minima and maxima of the histogram. Optimal thresholds are found at the minima of the statistical distribution resulting from the sum of the Gaussians.

The quality of segmentation is strongly limited by image resolution. In particular, the voxels containing microporosity appear as shades of gray and can be easily misclassified by a single thresholding technique,

since they make the ideal separation between the pore phase and the solid phase less clear. It may also happen that, in presence of microporosity, the stack histogram shows two peaks in the low intensity range. In this case, the pore space is identified by selecting the threshold value at the second minima of the stack histogram. The reason for this choice and the implications in terms of estimated porosity and permeability will be presented later on in this work (Sec. 4). However, it is important to highlight the fact that if microporosity is not described, not only total porosity is underestimated, but also connectivity. This strongly affects the estimations of the average pore diameter, average flow velocity, overall flux and other parameters sensitive to stagnant regions (Leu et al., 2014).

The application of the described four-step methodology have shown that, for the available datasets, morphological operation, e.g. erosion/dilation, were not necessary. These techniques are generally used when there are artifacts that need to be removed (Iassonov et al., 2009), or to find the skeleton of the pore space within a network modeling approach (Blunt et al., 2013). Obviously, when one wants to apply such morphological operations, the risk of indiscriminately removing not only spurious noise but also true features has to be considered.

2.2. Mesh generation

A voxel-based mesh generation strategy has been developed for creating the computational grid. A novel mesh generator has been implemented on the basis of the OpenFOAM® library to allow direct meshing on the denoised image stack. The meshing process is outlined in Fig. 1, where dotted blocks are optional. The process is automatic and faster, if compared to other approaches, because the final mesh is obtained without the need for extracting a Stereolithography (STL) representation of the pore-grain interface. The final mesh is obtained iteratively, by further refining the initial mesh.

Mesh generation starts from a cartesian background grid, which is superimposed on the 3D image stack domain. The initial cell size Δx_i is related to the image resolution *res* according to

$$\Delta x_i = res \cdot 2^N$$

so that at the *N*-th iteration it will be equal to the pixel size. At each iteration, the gray level statistics (minimum, maximum and average value) of the pixels contained in one cell is computed and associated to that cell. Local information about average gray are used for cell classification and for modeling the microporosity, as it will be explained in the next section. Cells are classified as fluid cells, solid cells or boundary cells, on the basis of the threshold chosen during the image processing phase. Solid cells are excluded from further analysis, while fluid and boundary cells are kept. Boundary cells are refined by splitting hexaedral cubic cells into eight. The process iterates until the pixel size is reached. Finally, the mesh is split into multiple regions and only connected paths are kept. The final mesh has a stair-step pattern (castellated mesh) and includes only fluid cells. Fig. 2 shows the refinement process over an initial background mesh with cubic cells of 64 pixel side.

Two additional steps can also be performed, namely throats refinement and smoothing. Throats refinement improves the accuracy of the numerical solution in the throats and narrow restrictions, where the flow speed is higher. It is not strictly required if, for example, the image has a high resolution, since the mesh has been generated with the minimum cell size of a pixel. On the other hand, if the resolution is low, throats may contain too few cells and the accuracy of numerical results may be affected. High speed regions can be identified, for example, by running a preliminary flow simulation with a potential flow solver, that will provide a first attempt solution to the velocity field. In fact, one can have an idea of where the main flow paths are by displaying the velocity field, even regardless of its actual magnitude. Once these critical regions are identified, refinement is achieved by splitting the cubic cells and/or by further refining near the walls. Fig. 3 examplifies the mesh refinement based on high speed region identification. Fig. 3a is an enlarged view of a 2D cut of a pore throat and displays the magnitude of the velocity field as it is obtained by running the preliminary potential flow simulation with a fixed inlet velocity of 1 mm/s. It is reasonable to assume that the high speed region consists of all red cells where the speed is greater or equal to ten times the Darcy inlet velocity. One level of volume refinement is applied to these cells, and one additional layer is added at the walls. The refined mesh is shown in Fig. 3b. The sensitivity of the calculated permeability on the refinement is discussed in Sec. 4. The second optional step is smoothing. The smoothing of the rock surface helps in getting a surface that is more realistic than a stair-step mesh. Mesh morphing is handled with the native OpenFOAM® mesh generator snappyHexMesh, so that mesh quality is ensured. Mesh smoothing requires the extraction of a STL surface from the castellated mesh. Since the proposed methodology avoids the creation of a surface reconstruction at image processing level, the surface should be created via an interpolation
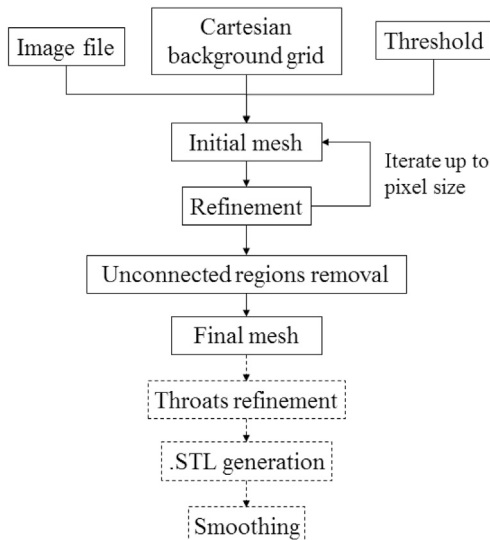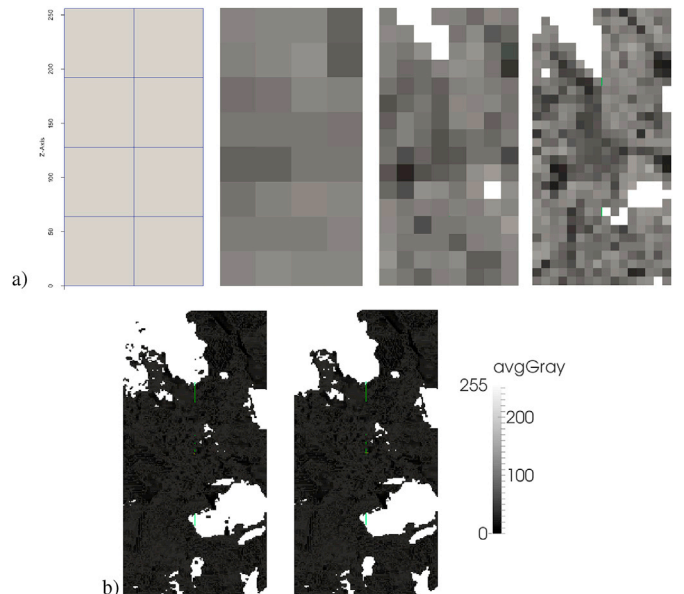
Fig. 1. Mesh generation.

Fig. 2. Mesh generation: (a) background mesh and first iterations of the refinement cycle (b) removal of unconnected regions and final mesh.
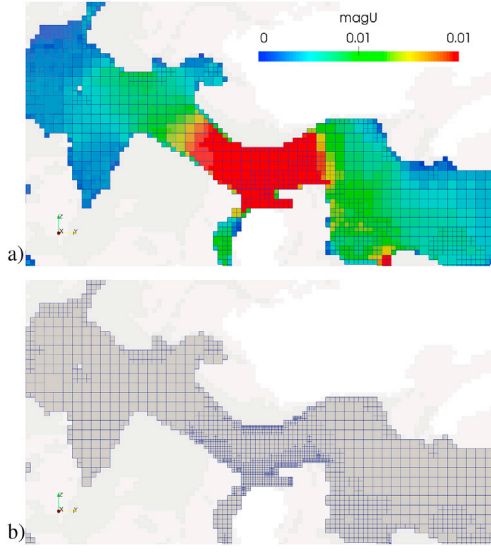
Fig. 3. Mesh refinement: (a) identification of high speed regions by a potential flow simulation (b) throat and wall refinement.

of the castellated mesh, which might be too expensive in terms of time and resources. For single-phase flows, drawbacks seem to overcome the gain in accuracy of the results. For this reason, mesh smoothing is avoided and simulations are run on the castellated mesh. In case of multiphase flow simulations, a step-like mesh requires special care, especially when capillary forces are evaluated (Raeini et al., 2012), but that is beyond the scope of the present paper.

2.3. CFD model

Conservations of mass and momentum are solved numerically for a single-phase, isothermal, steady flow of an incompressible, Newtonian fluid. Under these assumptions, the governing Navier-Stokes equations reduce to (Frisch, 1995):

$$\nabla \cdot \mathbf{u} = 0 \tag{1}$$

$$(\mathbf{u} \cdot \nabla)\mathbf{u} = \mathbf{g} - \nabla(p/\rho) + \nu \nabla^2 \mathbf{u} \tag{2}$$

where $\mathbf{u}$ is the flow velocity, p is the pressure, ρ is the fluid density, ν is the fluid kinematic viscosity, g is the gravitational acceleration and ∇ is the nabla operator. The system of Eqs. (1) and (2) can be further simplified by assuming creeping or Stokes flow conditions, which means that the left-hand side of Eq. (2) can be neglected.

The experimental set-up of a permeameter is reproduced by imposing a uniform fixed velocity at the inlet, along the longitudinal direction of the sample, namely the z-direction. The inlet value is set in order to grant creeping flow conditions. No-slip conditions are imposed at the walls. Under these assumptions, the absolute permeability can be computed from the Darcy law considering the pressure gradient estab-lished in the z-direction. The prediction can be directly compared with the experimental value corrected in order to take into account the Klinkenberg effect.

Reliable estimations of macroscopic quantities require the simulation of a sufficiently long sample. If the sample is too small, the solution is not representative, but if it is too long, heterogeneity effects may be too relevant. Mostaghimi et al. (2012) have found, as a rule of thumb, that the REV needed for flow-based measures is up to twice as large as the REV based on geometrical quantities, such as porosity or specific surface area (Mostaghimi et al., 2012). The dependency of absolute permeability on sample length has been investigated, while keeping the cross-sectional area constant. This corresponds to the assumption that permeability is

more sensitive to a change in length than to change in cross-section, which seems reasonable if the aspect ratio (length to width) is not excessive.

Fluid-dynamic permeability is very sensitive to an arbitrary choice of the threshold (Leu et al., 2014). If the threshold value is high, perme-ability may be overestimated; if it is too strict, full path connectivity may not be ensured. With a finite resolution, the assumption that all computational fluid cells are completely empty (open-pores) has no physical basis. Pixel intensities depend on the presence of microporosity, so it is possible to identify microporous regions and treat them accordingly. In the proposed approach, unresolved porosity regions have been included in the pore space, mimicking their presence with an increased fluid resistance. A local resistivity source term, $\mathbf{R}$, has been included in the conservation of momentum (Eq. (2)) as a generic Darcy resistance term (Dullien, 2012):

$$\mathbf{R} = \nu d_i \mathbf{u} \tag{3}$$

where d_i is a resistivity factor associated to the microporosity. In the proposed simplified model, d_i is computed as a linear function of the average grayscale level g_i associated to each cell. For example, to apply the model in the range $[g_{min}, g_{max}]$, the resistivity factor is defined for each cell i as:

$$d_i = \begin{cases} 0, & \text{if } g_i < g_{min} \\ \dfrac{d_{max}}{g_{max} - g_{min}}(g_i - g_{min}), & \text{if } g_{min} \leq g_i \leq g_{max} \\ d_{max}, & \text{if } g_i > g_{max} \end{cases}$$

The grayscale range $[g_{min}, g_{max}]$ defines the region in which microporosity is present and it can be identified on the basis of the analysis of the histogram of the image, considering the region of transition between open pores and solid media. As it will be exemplified in the following sections, a reasonable criterion is to assign g_{min} to the gray level of the peak associated to the open pores and g_{max} to the threshold value adopted for the image segmentation.

3. Dataset

The considered datasets consist of 3D stack of images of four samples obtained from X-ray microtomography. Image resolution and dimensions are reported in Table 1. For each sample, the experimental value for the helium effective porosity and absolute gas permeability is available from measurements performed at eni laboratories (see Table 2). Datasets S1 and S2 refer to sandstones, which are characterized by an experimental value of permeability that is two orders of magnitude higher than for datasets T1 and T2. Scanning Electron Microscopy (SEM) and mercury porosimetry results have highlighted that T1, T2 and S2 contain a high percentage of microporosity due to clays.

4. Results and discussion

Results for the geometrical and fluid-dynamic characterization of the four samples are presented. These include the evaluation of the total and connected porosity Φ, the specific surface S_{sp}, the equivalent pore size D_{eq}, the absolute permeability k along the longitudinal axis and the tor-tuosity τ.

Table 3 collects the final results for all the samples presented in Table 1. In particular, for sample S1 three tomographic acquisitions have been made to investigate the presence of significant heterogeneity at the plug scale.

4.1. Geometrical characterization

The geometrical characterization follows the workflow described in the previous sections. Image processing is exemplified considering a

Table 1
Resolution per pixel of the micro-CT images.

	Resolution (µm)	Dimensions (pix)
Tight rock 1, T1	2.175	700 × 700 × 2444
Tight rock 2, T2	2.73	1292 × 1292 × 1600
Sandstone 1, S1	2.13	992 × 1015 × 992
Sandstone 2, S2	2.05	988 × 1015 × 992

Table 2
Experimental data for helium effective porosity and absolute gas permeability.

	Porosity (%)	Permeability (md)
Tight 1, T1	10.6	0.4
Tight 2, T2	12.7	0.5
Sandstone 1, S1	20.3	60
Sandstone 2, S2	16.6	55

Table 3
Summary of the results for the geometrical and fluid-dynamic characterization of the available samples. Cropped dimensions: T1 512 × 512 × 1600, T2 512 × 512 × 1024, S1 512 × 512 × 512, S2 512 × 512 × 896.

	Nb. cells (MLN)	Φ_{conn} (%)	S_{sp} (1/mm)	D_{eq} (µm)	k (md)	τ (−)
T1	19.1	8.0	42.1	7.5	0.6	2.3
T2	15.5	12.8	38.6	13.2	1.8	2.1
S1-a	10.0	21.1	53.9	15.7	529	1.5
S1-b	9.7	9.4	59.8	5.5	6.6	2.0
S1-c	13.8	25.5	61.7	16.4	1202	1.4
S2	16.0	16.6	58.4	11.4	60.6	1.7

centred subsample of T1, having a squared cross-section of 512 × 512 pixels and a total length of 1600.

Fig. 4a–b shows how the histogram associated to the image stack appears before and after being digitally processed. Fig. 4a is the original stack histogram of the 8-bit centred subsample of T1. Intensities range from 0 (black) to 255 (white). Lighter gray values correspond to solid mineral phases, darker gray values to pores. Peaks identify phases having a similar attenuation coefficient. It can be noticed that, if the image stack is not processed, contrast is too poor and peaks cannot be distinguished. Fig. 4b shows the stack histogram after contrast enhancement and denoising. Gray values are well distributed over the entire range of intensities and minima for thresholding can be clearly identified. Compared to bilateral filtering (BF), non-local means (NLM) produces higher maxima and lower minima. The pore space distribution retrieved with bilateral filter is bell-shaped, whereas with non-local means it is right-skewed and resembles a lognormal distribution. This suggests that the blurring effect introduced by bilateral filter is more pronounced. Anyway, the location of the first minimum, that identifies the threshold between pores and solid, remains unchanged, taking the value of 46 for

BF and 45 for NLM. The corresponding value for the total porosity is slightly higher for NLM (9.2% against 8.0% with BF). Peak signal-to-noise ratio (PSNR) and structural similarity (SSIM) (Wang and Bovik, 2002) have been evaluated to assess the quality of denoising in a quantitative way. With the current parameter setting, the dataset processed with NLM has an associated PSNR that is slightly higher, suggesting a better performance in terms of denoising. The SSIM index for both filters is greater than 0.9, so structural information are not excessively distorted. For gaussian-like data distributions, it is also possible to estimate mode locations using a mixture model (Huang and Chau, 2008). Soft, or probabilistic, ownerships may perform better with respect to hard assignments in case of nearby peaks. Fig. 4c shows the Gaussian Mixture Model that fits the histogram processed by BF. In this example, data have been clustered using a mixture of four Gauss distributions, one for each detectable peak. The maximum likelihood parameters of the fitting distributions have been obtained using the Expectation Maximization algorithm, under the assumption that each mode corresponds to a normal distribution. The GMM thresholding approach results in lower values of threshold (40) and total porosity (7.1%).

For the geometrical characterization to be reliable, a Representative Elementary Volume (REV) of the sample shall be considered. Once the threshold is selected, the size of the REV is calculated by increasing the sample length, while keeping fixed its cross-section. For each length, the total porosity of the subsample is evaluated. Fig. 5a shows that, after an initial decrease, the total porosity remains almost constant for sample lengths exceeding 0.6 mm (9.2% ± 0.5). A change of one percentage point can be regarded as acceptable, because it lies within the experimental error. The local porosity value of each slice gives an idea of the heterogeneity within the sample (see Fig. 5b). If the same procedure is applied to a sample having a smaller cross-section, the estimated REV length will not be the same. However, this difference has been verified to be negligible for static properties estimation. On the contrary, for dynamic properties like permeability, a larger cross-section may provide a better connection of the flow paths. This issue will be further discussed later on. For the tight rock T1, SEM images with a resolution of 0.16 microns were also available. Thus, it has been possible to conduct a deeper investigation on the limits of resolution when trying to characterize a tight sample. Fig. 6a shows a representative detail for the sample in the original SEM, with the relative histogram reported in Fig. 7. Three types of porosities are clearly distinguishable: open pores, intergranular porosity and a clay-rich microporous region. Open pores are highlighted in blue in Fig. 6c and correspond to the first mode of the histogram. The intergranular porosity and the clay-rich microporous region, highlighted in red in Fig. 6e, correspond to middle grays. Intergranular porosity is made of tiny slot-like pores along grain boundaries, whose relative contribution to the porosity appears to be smaller than that of the clay-filled pores. It can be also noticed that the clay-rich region provides direct connection between the two open pores shown in Fig. 6c, which might play a role in the definition of the preferential flow paths. Recent
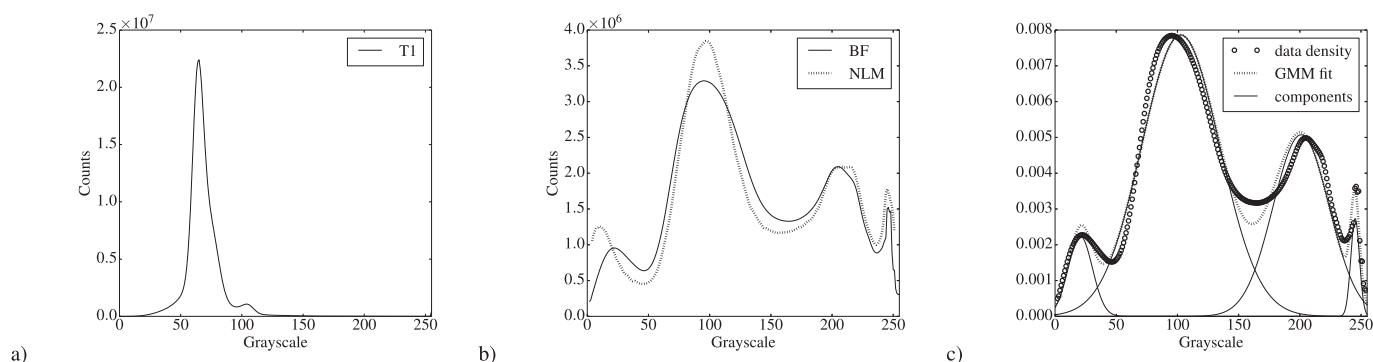

Fig. 4. Image processing - effects on the stack histogram of a 512 × 512 cropped sample: a) original; b) after contrast enhancement and bilateral filtering/non-local means; c) gaussian mixture fitting.
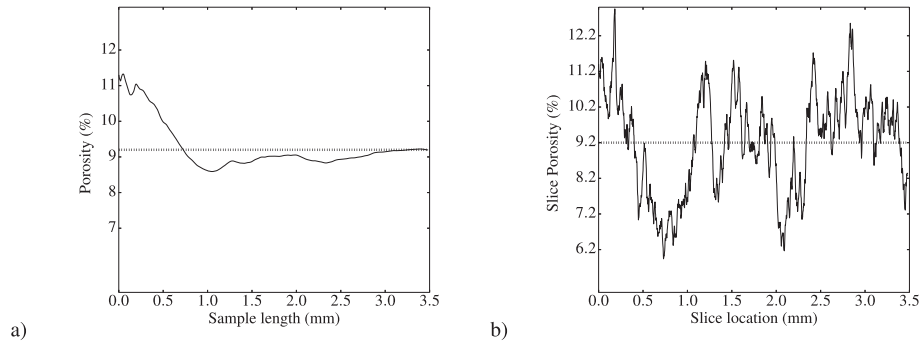
Fig. 5. REV for static properties: total porosity for a sample of increasing length (a); porosity as a function of the longitudinal axis (b). Average values (dotted lines) refer to the total porosity of the whole sample (9.2%).
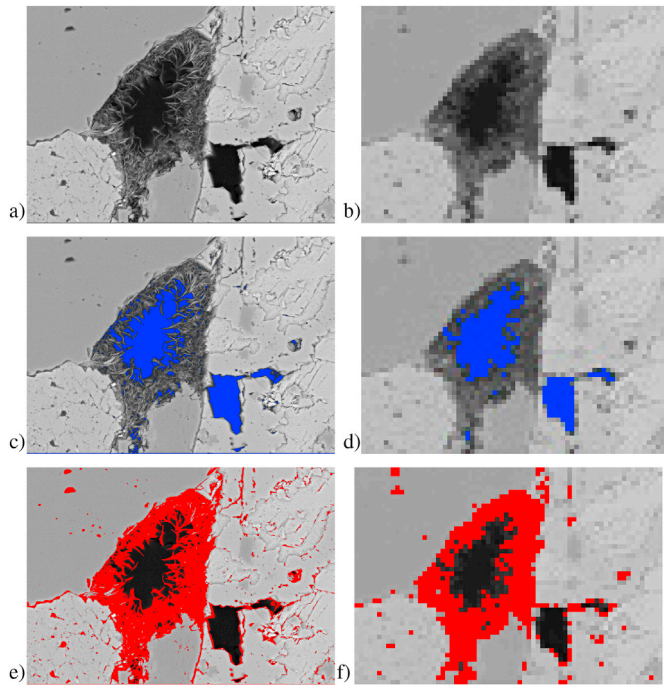

Fig. 6. Open pores and microporosity in SEM (a)-(c)-(e), 0.16μm/pix, and low-resolution SEM (b)-(d)-(f), 2.4μm/pix. Original images (a)–(b); open pores (c)–(d), 8.0% porosity; microporous region (e)–(f), 18.4% porosity.

Fig. 7. Histogram of the SEM image (0.16μm/pix): open pore region in blue, microporous region in red. (For interpretation of the references to colour in this figure legend, the reader is referred to the web version of this article.)

studies in tight gas sandstones suggest that clay-filled microporosity, and not slot-like pores, is the most important flow path (Golab et al., 2010). Lower-resolution images have been constructed from the original SEM images by pixel averaging (see Fig. 6b), so that the final resolution (2.4 μm) is comparable to that of the tomographic acquisition. Then, open pores and microporous regions have been identified by visual in-spection (Fig. 6d-f). By comparing Fig. 6c with Fig. 6d, it can be inferred that open pores are satisfactorily well-resolved at both resolutions; on the contrary, the morphological structures of the slot-like pores and of the clay features are completely lost (Fig. 6f). Nonetheless, as long as clay-filled pores are included in the segmentation, connectivity seems to be ensured. This result is further discussed in the next section, where a threshold-sensitivity analysis is performed to highlight the role of microporosity in providing connectivity of the flow paths and better es-timations for porosity and permeability.

Geometrical properties are computed once the mesh has been generated and after non-connected regions are removed. The analysis aims at quantifying the connected porosity, the specific surface and the average pore size. The computation of the connected porosity Φ_{conn} and specific surface S_{sp} is straightforward by the definition. The former is defined as the ratio between the pore volume that can be accessed by the
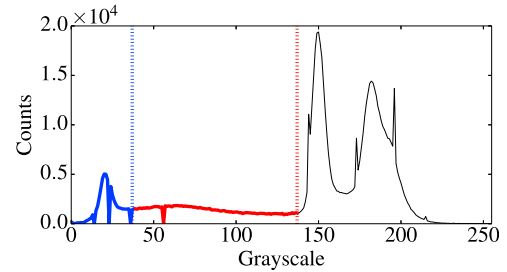
flowing fluid and the total (bulk) volume of the considered test section. The latter is given by the ratio between the surface area at the walls and the total (bulk) volume of the considered test section. In order to estimate the average pore size, the pore space morphology has been analyzed using the maximum inscribed sphere method (Silin and Patzek, 2006). This approach relies on the description of the pore space via clusters of inscribed spheres and has been proven to be effective in pore networks extraction from tomographic images (Dong and Blunt, 2009). Therefore, it has been developed and implemented in the OpenFOAM®, to be used as a post processing tool. At first, the entire domain is explored to find the range of all possible values of the radii of the maximal spheres. Since each sphere is cell-centred and shall touch the solid surface, the range will be limited by the minimum and maximum distances, over the entire domain, between the cell centre and the nearest wall (Fig. 8a). Starting from the largest possible sphere, increasingly smaller spheres are built and if two of them touch, they are merged and clustered (Fig. 8b). It must be remarked that in order to cope with the step-like discrete represen-tation of the sphere, it is advisable to adopt a lower and upper limit for the radius of the sphere, instead of one value only. At the end of the process, the entire pore volume is filled and an average pore diameter can be obtained analyzing the size distribution of the sphere radii. In particular, the average pore diameter has been calculated as a volume-weighted average, so that the relative contribution of each diameter is given by the percentual volume of occupation of the sphere. Then, this value is compared to a theoretical estimation of the equivalent diameter $D_{eq} = 4V_{pore}/S$, obtained assuming that the pore space is reduced to an equivalent capillary tube of volume V_{pore} and surface area S.

The aforementioned geometrical characterization is here exemplified for a cropped sample of S1, having a cross-section of 256 $\times$ 256 pixels. For this sample, the pore space has been identified in the range of in-tensities 0 to 67 (see the stack histogram reported in Fig. 9). From Fig. 9 it can be also noticed that the pore distribution is narrow, suggesting that pores are well resolved. The representativeness of the sample is checked by considering different lengths. From Table 4 it can be noticed that a test
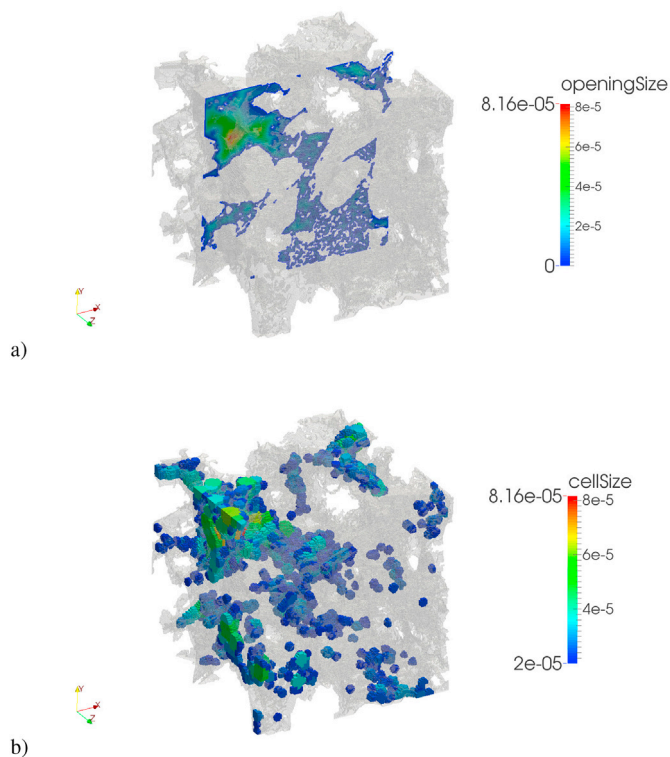
a)

b)

Fig. 8. Pore space morphology analysis, S1 (256 × 256 × 256): visualizations of the maximum distance from the wall (a) and of the spheres filling the pore space (b).

section of 0.3 mm long is sufficient to capture the porosity and specific surface. In the same table, values for the total porosity Φ_{tot} are provided and refer to the estimation of the porosity before the removal of the unconnected regions from the mesh. For this sample, the difference between the total and connected porosity is negligible, suggesting that the pore space is well connected. The maximum inscribed sphere method applied to this sample gives an average pore diameter of 17 microns, which is in good agreement with the theoretical equivalent diameter (16 microns). This result seems reasonable, as it aligns with the literature studies upon the validity of a capillary tube model for sands.

4.2. Fluid-dynamic characterization

The fluid-dynamic characterization of the samples includes the estimation of their absolute permeability and tortuosity. CFD simulations are carried out on the 3D finite volume open-source platform OpenFOAM®. If not stated otherwise, no additional refinement has been applied to the base mesh having cell size equal to pixel size.

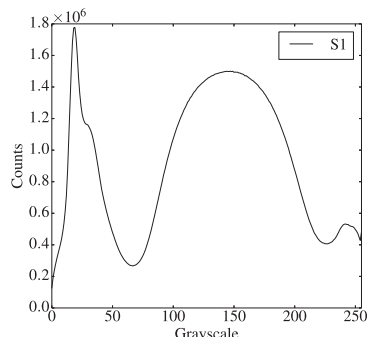The governing equations have been solved imposing a fixed inlet

Fig. 9. Stack histogram of S1, NLM denoising applied.

Table 4
Geometrical characterization of S1. Centred cropped sample, squared cross-section 256 × 256. Dependency on the test section length.

Length (pix)	S_{sp} (1/mm)	Φ_{tot} (%)	Φ_{conn} (%)
128	59.1	26.3	26.2
256	57.6	24.5	24.4
384	58.9	23.9	23.8
512	59.7	23.4	23.2
640	60.0	22.4	22.3
768	57.8	22.1	21.9

value for the velocity, a fixed reference pressure at the outlet, no slip and zero pressure gradient at the walls. Permeability values are retrieved from the Darcy equation. So, in order to ensure a Darcy regime, all the calculations have been performed setting the inlet velocity to 1 mm/s. This value has been selected after comparing the results obtained from the basic steady-state solver for incompressible flows to those obtained from a Stokes solver, where inertial terms have been removed from the equations. As shown in Table 5, the absolute permeability retrieved by imposing 1 mm/s (k@1 mm/s) differs from that obtained under Stokes flow conditions (k_{stokes}) for less than 1%. It must be noticed that Table 5 refers to simulations that do not take into account a model for microporosity, i.e. microporous region are considered as open pores; therefore, the reported permeability values are far from being a reliable estimation for the tight sample under analysis. Considering that microporous regions are mainly located around the open pores and that they represent a resistance term (see Sect. 2.3), when microporosity is included in the analysis the flow experiences an increase in velocity due to a reduction in the effective cross-section area. Even so, the calculated Reynolds number is less than 1, meaning that the flow regime is still laminar and the Darcy regime assumption holds.

A mesh sensitivity analysis has been undertaken to test the need for further refinement in high velocity regions. Throat refinement has been performed as detailed in Section 2.2. Fig. 10 is an enlarged view of a longitudinal slice of the sample in a high speed region. Fig. 10-a displays the solution for the velocity field on the base mesh, while Fig. 10-b is the solution obtained for the refined mesh. As expected, refinement improves the velocity profile near the walls, but the maximum value is correctly predicted in both cases. The estimated values for absolute permeability have been collected in Fig. 11. For this sample, refinement has a negli-gible effect on the accuracy of the results, with a calculated maximum percentage error of 1.5%.

In order to perform a sensitivity analysis on the REV size, sample dimensions and position have been sistematically changed and results have been collected in Figs. 11 and 12b. Fig. 11 is an example of REV analysis performed on a subsample of S1, where absolute permeability is computed considering different sample lengths and a fixed cross-section (256 × 256). It can be noticed how permeability decreases for increasing sample length, until it approaches an almost constant value for samples longer than 0.8 mm. This trend is actually confirming the expectations. In particular, if the sample is very short, inlet and outlet patches are very close to each other, the number of almost-straight flow paths connecting them is higher and, therefore, permeability is higher. On the contrary, in a longer sample tortuosity is favored and some lateral flow paths may be lost, decreasing permeability. In this example, a sample that is 0.8 mm

Table 5
T2 cropped sample, 256 × 256. No subgrid model is applied. Sensitivity on the inlet value for the velocity.

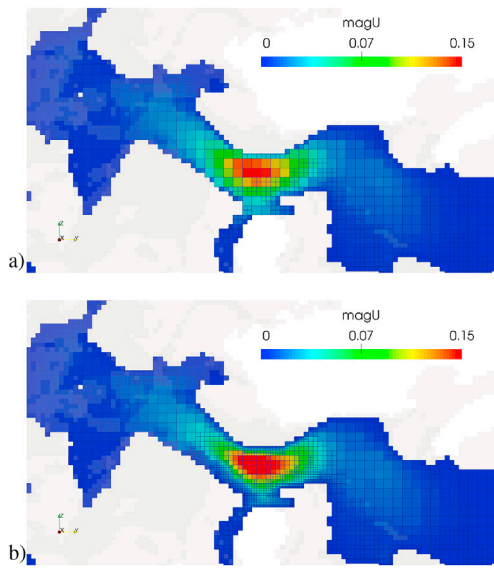| Length (pix)	k_{stokes} (md)	k@1 mm/s (md)
512	94	93
768	112	111
1024	112	111
1280	120	119
1536	98	97

Fig. 10. Effect of the refinement on the velocity field in a high velocity region.
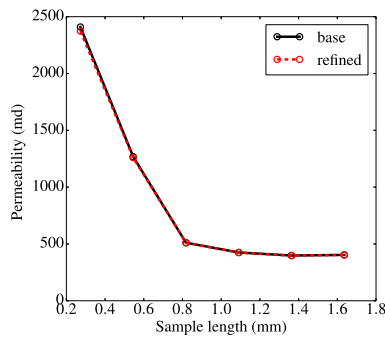

Fig. 11. REV for dynamic properties, S1 (256 × 256): permeability as a function of the longitudinal axis and effect of mesh refinement.

long can be regarded as a representative one, confirming that the REV for permeability estimations is bigger than that obtained for static properties (refer to Table 4).

Furthermore, the effect of sample position and cross-section has been investigated. Fig. 12 shows REV analysis performed on three different subsamples of T2. Their location is depicted in Fig. 12a: sample A and B (yellow) have a squared cross-section of 0.7 mm-side, while sample C (red) has a squared cross-section of 1.4 mm-side. The initial decrease in
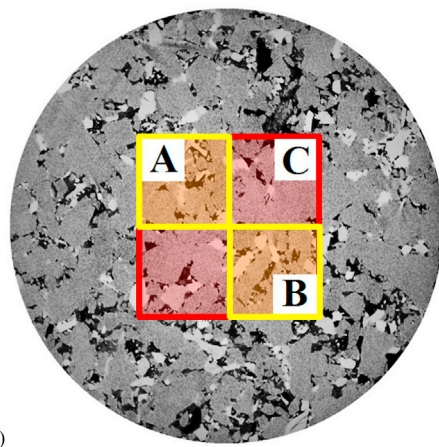
permeability is very pronounced for sample A. For sample B and C, permeability reaches a constant value at approximately 1.5 mm (150 md for B, 174 md for C). On average, sample A is tighter (93 md@1.5 mm, 111 md@2.1 mm). It has to be remarked that these estimations do not take into account the subgrid model for microporosity. For sample A, permeability remains constant up to 4.0 mm; whereas, for sample B, it further decreases when the sample is longer than 2.8 mm. This suggests that sample B is more heterogeneous than sample A. For the considered sample, cross-section size and position does not affect to a great extent the constant value reached by permeability, at least for what concerns the order of magnitude. The exact value depends on both of them, since some main flow path may be excluded or interrupted.

Since the values of permeability for T2 overestimate the experimental measures up to two order of magnitude, sensitivity analysis on threshold choice has been performed. In particular, the pore distribution has been first identified on the image histogram by the minimum criteria (Fig. 13a, and then threshold has been varied within the corresponding gray intensity range (0 60). The segmentation at the lowest threshold value that has been considered (20) includes only the open pores, as shown in Fig. 13b, and yields to an unconnected domain. For higher threshold values sub-resolution pores, that are characterized by an intermediate gray-level between open pores and solid phase (Fig. 13c), are also included in the segmentation and the pore space is found to be con-nected. Porosity and permeability results have been collected in Table 6. It can be noticed that open pores account for less than half of the experimental porosity. Comparing total and effective porosity, the dif-ference between the two values decreases increasing the threshold value, meaning that the flow paths connectivity is improved. Results for permeability are consistent with the fact that in these simulations the microporosity model has not been applied: indeed, micropores have been included in the domain without considering that they provide an addi-tional fluid-dynamic resistance compared to the open pores.

Fig. 14 shows in red corrected permeability values for T1, T2 and S2 obtained with the introduction of the subgrid linear model for micro-porosity. The model is applied in the gray intensity range delimited by the first maxima and the first minima of the denoised stack histogram. For example, in case of the sample T2, whose histogram is reported in Fig. 13 a, the grayscale range for the application of the subgrid model is $[g_{min} = 20, g_{max} = 60]$. On the other hand, in the range between 0 and the first maximum, pores are fully open and, therefore, subgrid model is not required.

Fig. 15 is a cut of the T2 sample, showing how the local resistivity values changes according to the average gray value of the cells. Re-sistivity d_i is null for open pores, then increases linearly in the micro-porous region up to a certain value, namely d_{max}. Theoretically, d_{max} would represent the resistivity of the solid phase or the inverse of its permeability, so it is potentially infinite. In practice, d_{max} is a parameter
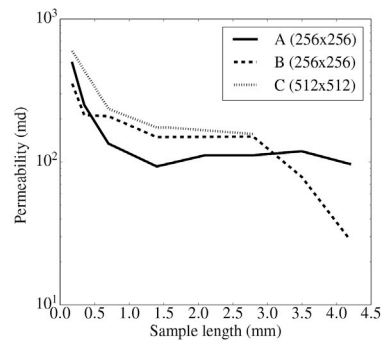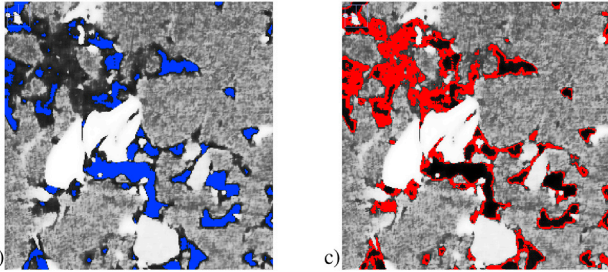

Fig. 12. REV for dynamic properties, T2: sensitivity analysis on sample position and cross-section. No subgrid model is applied.
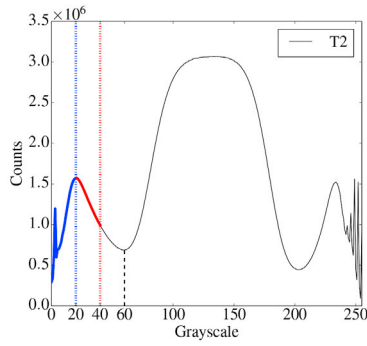
Fig. 13. T2 cropped sample, 512 × 512 × 1536. Stack histogram (a) and details of the segmentation (b–c). Grayscale ranges: 0–20 (b); 21:40 (c).

Table 6
T2 cropped sample, 512 × 512 × 1536. No subgrid model is applied. Porosity and absolute permeability dependence on threshold.

Threshold	Φ_{tot} (%)	Φ_{conn} (%)	k (md)
20	5.1	–	–
25	6.9	5.5	2.3
30	8.6	7.6	12.4
40	11.3	10.6	50.9

that controls the mean value of the resistivity of the microporous region. Therefore, one option is to set d_{max} in order to retrieve a permeability value for microporosity that is consistent with those available from literature correlations for clays derived from nanoporous structural models (Long et al., 2013). Obviously, the other option is to set d_{max} to match directly the laboratory measurements for the sample that is under analysis. Table 7 summarizes the effect of different d_{max} settings on permeability estimations for T2 (256 × 256 × 768). Without the subgrid model, numerical predictions are higher than the experimental value by two orders of magnitude. As expected, permeability decreases with increasing d_{max}.
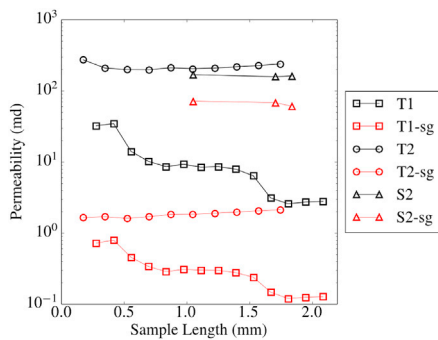

Fig. 14. Permeability correction by a subgrid linear model for microporosity. Initial predictions are shown in black, red values are obtained when the subgrid (sg) model is applied ($d_{max} = 1e+ 13$ m^{-2}). Subsamples dimensions: 256 × 256 for T1/T2, 512 × 512 for S2. Graylevel range of application [min,max]: [22,47] for T1, [20,60] for T2, [25,54] for S2. (For interpretation of the references to colour in this figure legend, the reader is referred to the web version of this article.)
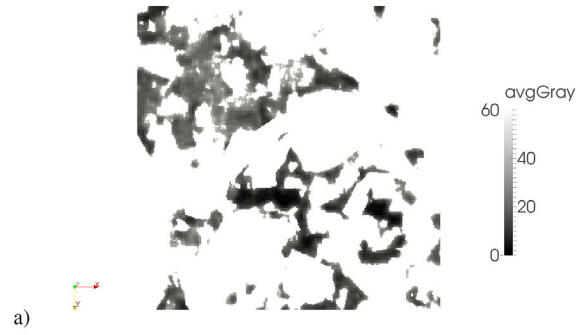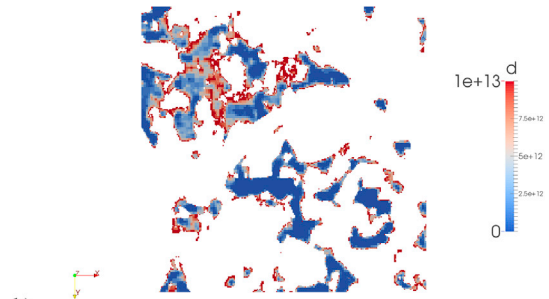
Fig. 15. Microporosity modeling in sample T2: (a) average gray field; (b) local resistivity value computed on the basis of a linear model. Open pores, in black, have a null resistivity.

Table 7 includes also results on tortuosity. Tortuosity (τ) is a measure of pore connectivity and requires the estimation of the effective elongation of the flow paths. Finding streamlines can be a non-trivial, time consuming and error-prone task even in relatively simple system (Matyka et al., 2008). In order to avoid any issue of having incomplete streamlines or in dealing with dead-end pores, tortuosity has been calculated from the velocity field, as proposed in Duda et al. (2011)

$$\tau = \frac{\langle u \rangle}{\langle u_z \rangle}$$

where $\langle \cdot \rangle$ stands for the volumetric average, u is the magnitude of the velocity field and u_z the component along the macroscopic flow direction. This definition includes recirculation effects and edge effects. Results for T2 show that the proposed approach consistently reproduces the role of microporosity in affecting the tortuosity of the flow paths.

4.3. Validation

Table 3 collects the average numerical predictions obtained for representative subvolumes of the rock samples. Numerical predictions for porosity and absolute permeability are in good agreement with experimental values. In particular, the application of the proposed segmentation strategy has led to porosity estimations that are within the experimental error, without any special issue in their determination. On the contrary, the estimation of the absolute permeability is more critical, with initial numerical predictions that were overestimating experimental data by a factor of 10 or more. For three of the four analyzed samples (S2,

Table 7
Subgrid linear model: sensitivity on the selected value for the maximum resistivity. Non-corrected values: $k = 180$md, $\tau = 1.7$.

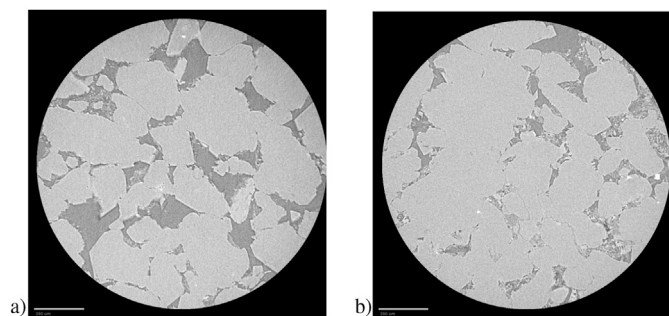| d_{max} (m^{-2})	k (md)	τ
1e+13	20.9	1.84
1e+14	4.4	1.96
1e+15	0.7	2.04
1e+16	0.08	2.07

Fig. 16. Heterogeneity effects: tomographic acquisitions of S1 in a high permeable layer (a) and in a low permeable layer (b).

T1, T2), SEM images have confirmed that the mismatch is due to the presence of micropores, whose size is such that they cannot be resolved at the tomographic resolution. In these cases, the application of the proposed subgrid model has been necessary to predict the measured order of magnitude of the absolute permeability. On the other hand, for S1 (S1-a) the mismatch is due to the presence of heterogeneity at the plug scale, that makes numerical and experimental values not comparable, since measurements and simulations are performed at different scales. As a matter of fact, simulations have been performed on a reconstructed volume of about 2 cubic millimeters, while experiments are made on a much longer core plug, where the less permeable layers strongly affect the fluid flow.

In order to support the experimental observations about the layered structure of S1, multiple microtomographic acquisitions have been made at different locations of the plug, within a lower permeable layer (S1-b) and a higher permeable layer (S1-c). From Fig. 16 it is evident that in S1-c open pores are wider and more well distributed. The average effective porosity for this sample is about 25%, with a predicted absolute permeability of 1.2 d (sample S1-c in Table 3) that is 200 times higher than the value obtained for S1-b. The application of the proposed subgrid model on S1-b and S1-c has a negligible effect over permeability predictions, confirming that the inner structure is well resolved and that heterogeneity is the main responsible for the deviations from the experimental measurements.

4.4. Computational time

Fig. 17 shows the simulation CPU time as a function of the number of cells, i.e. increasing representative volumes, for a low and a high permeable sample. Decomposed cases are run on 4 processors Intel® Core™ i7 CPU 860@2.80GHz. Base meshes have been generated without further throats refinement. In refined meshes, high speed regions have been refined by one level in the volume and one level near the walls. As
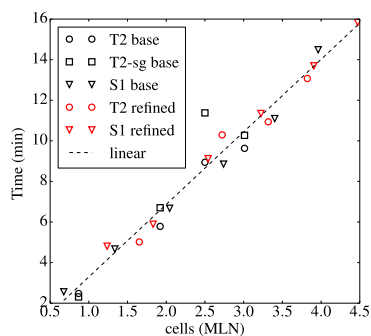
expected, the run time increases linearly with the number of cells. For these simulations, the application of the subgrid model is associated to a slightly increased computational time.

5. Conclusion

A complete workflow has been proposed to predict rock properties for sandstones and tight rocks. The implications of having a limited resolution in the tomographic images have been investigated, with particular attention to the presence of rock microporosity. Despite clay features cannot be resolved, a histogram-based thresholding strategy combined with the introduction of a resistivity source term in the governing equations have produced encouraging results. In particular, predictions of the effective porosity and absolute permeability are consistent with the experimental data.

A novel meshing strategy has been developed in OpenFOAM® to allow direct meshing on the denoised image stack, with the advantage of being automatic and fast. As a matter of fact, the time spent for mesh generation is 10–20% of the total time taken by the entire workflow, which is a small percentage considering that single-phase steady-state flow simulations are quite fast (order of mins or hour); moreover, this time can be regarded as negligible when more time-consuming transient multi-phase flow simulations are addressed. Furthermore, the possibility of refining the mesh inside throats and narrow restrictions allows to reach a compromise between the quality of the results and the cost, in terms of time and resources.

CFD single-phase flow simulations have been performed to compute geometrical and fluid-dynamic properties of four different samples. The dependence of rock properties on the quality of the segmentation, on the size and the position of the REV has been investigated. For all samples, effective porosity estimations show a reasonable agreement with laboratory measurements. For tight samples and sandstones containing a high percentage of clays, microporosity contributes both in increasing the connectivity and in increasing the resistance to the fluid flow. If only the first one is considered, it has been found that predictions of absolute permeability can exceed experimental values by orders of magnitude. The application of the proposed model for subgrid porosity leads to more reliable predictions. It is possible to calibrate the model on the basis of literature correlations available for specific clay types thanks to multiscale imaging approaches. Future works may investigate the presence of different types of microporosities, for example by coupling information from microtomography and SEM.

Fig. 17. Effect of mesh size on CPU time for a high permeable sample (S1-a) and a low permeable (T2) sample on base meshes, refined meshes and considering the application of the subgrid model (sg).

References

American Association of Petroleum Geologists, 2015. Unconventional energy resources: 2015 review. Nat. Resour. Res. ISSN: 1573-8981 24 (4), 443–508. http://dx.doi.org/10.1007/s11053-015-9288-6.

Andrä, H., Combaret, N., Dvorkin, J., Glatt, E., Han, J., Kabel, M., Keehm, Y., Krzikalla, F., Lee, M., Madonna, C., Marsh, M., Mukerji, T., Saenger, E.H., Sain, R., Saxena, N., Ricker, S., Wiegmann, A., Zhan, X., 2013b. Digital rock physics benchmarkspart i: imaging and segmentation. Comput. Geosci. ISSN: 0098-3004 50, 25–32. http://dx.doi.org/10.1016/j.cageo.2012.09.005.

Andrä, H., Combaret, N., Dvorkin, J., Glatt, E., Han, J., Kabel, M., Keehm, Y., Krzikalla, F., Lee, M., Madonna, C., Marsh, M., Mukerji, T., Saenger, E.H., Sain, R., Saxena, N., Ricker, S., Wiegmann, A., Zhan, X., 2013a. Digital rock physics benchmarkspart ii: computing effective properties. Comput. Geosci. ISSN: 0098-3004 50, 33–43. http://dx.doi.org/10.1016/j.cageo.2012.09.008.

Awang, M., Negash, B.M., Akhir, N.A.M., Lubis, L.A., 2015. In: ICIPEG 2014: Proceedings of the International Conference on Integrated Petroleum Engineering and Geosciences. Springer.

Blunt, M.J., Bijeljic, B., Dong, H., Gharbi, O., Iglauer, S., Mostaghimi, P., Paluszny, A., Pentland, C., 2013. Pore-scale imaging and modelling. Adv. Water Resour. ISSN: 0309-1708 51, 197–216. http://dx.doi.org/10.1016/j.advwatres.2012.03.003, 35th Year Anniversary Issue.

Bradski, G., et al., 2000. The opencv library. Dr. Dobbs J. 25 (11), 120–126.

Buades, A., Coll, B., Morel, J.-M., 2005. A non-local algorithm for image denoising. In: Computer Vision and Pattern Recognition, 2005. CVPR 2005. IEEE Computer Society Conference on, vol. 2. IEEE, pp. 60 65.

Dempster, A.P., Laird, N.M., Rubin, D.B., 1977. Maximum likelihood from incomplete data via the em algorithm. Journal of the royal statistical society. Ser. B Methodol. 1–38.

Dong, H., Blunt, M.J., 2009. Pore-network extraction from micro-computerized-tomography images. Phys. Rev. E 80 (3), 036307.

Duda, A., Koza, Z., Matyka, M., 2011. Hydraulic tortuosity in arbitrary porous media flow. Phys. Rev. E 84 (3), 036319.

Dullien, F.A., 2012. Porous Media: Fluid Transport and Pore Structure. Academic press.

Easwaran, S., 2009. Simplified Teaching and Understanding of Histogram Equalization in Digital Image Processing. American Society for Engineering Education.

Eibenberger, E., Borsdorf, A., Wimmer, A., Hornegger, J., 2008. Edge-preserving denoising for segmentation in ct-images. In: Bildverarbeitung für die Medizin 2008. Springer, pp. 257–261.

Fredrich, J.T., Lakshtanov, D., Lane, N., Liu, E.B., Natarajan, C., Ni, D.M., Toms, J., et al., 2014. Digital rocks: developing an emerging technology through to a proven capability deployed in the business. In: SPE Annual Technical Conference and Exhibition. Society of Petroleum Engineers.

Frisch, U., 1995. Turbulence: the Legacy of A.N. Kolmogorov.

Golab, A.N., Knackstedt, M.A., Averdunk, H., Senden, T., Butcher, A.R., Jaime, P., 2010. 3d porosity and mineralogy characterization in tight gas sandstones. Lead. Edge 29 (12), 1476−1483.

Huang, Z.K., Chau, K.W., 2008. A new image thresholding method based on gaussian mixture model. Appl. Math. Comput. 205, 899 907.

Iassonov, P., Gebrenegus, T., Tuller, M., 2009. Segmentation of x-ray computed tomography images of porous materials: a crucial step for characterization and quantitative analysis of pore structures. Water Resour. Res. 45 (W09415) http://dx.doi.org/10.1029/2009WR008087.

Leu, L., Berg, S., Enzmann, F., Armstrong, R., Kersten, M., 2014. Fast x-ray micro-tomography of multiphase flow in berea sandstone: a sensitivity study on image processing. Transp. Porous Media. ISSN: 0169-3913 105 (2), 451–469. http://dx.doi.org/10.1007/s11242-014-0378-4.

Long, H., Nardi, C., Idowu, N., Carnerup, A., Øren, P., Knackstedt, M., Varslot, T., Sok, R., Lithicon, A., 2013. Multi-scale imaging and modeling workflow to capture and characterize microporosity in sandstone. In: International Symposium of the Society of Core Analysts, Napa Valley, California, USA page 13.

Matyka, M., Khalili, A., Koza, Z., 2008. Tortuosity-porosity relation in porous media flow. Phys. Rev. E 78 (2), 026306.

McLachlan, G., Krishnan, T., 2007. The EM Algorithm and Extensions, vol. 382. John Wiley & Sons.

Mostaghimi, P., Blunt, M.J., Bijeljic, B., 2012. Computations of Absolute Permeability on Micro-ct Images. International Association for Mathematical Geosciences. http://dx.doi.org/10.1007/s1104-012-9431-4.

OpenFOAM Foundation. OpenFOAM documentation. Avaiable from: http://www.openfoam.org/docs/.

Raeini, A.Q., Blunt, M.J., Bijeljic, B., 2012. Modelling two-phase flow in porous media at the pore scale using the volume-of-fluid method. J. Comput. Phys. 231 (17), 5653-5668.

Schindelin, J., Arganda-Carreras, I., Frise, E., Kaynig, V., Longair, M., Pietzsch, T., Preibisch, S., Rueden, C., Saalfeld, S., Schmid, B., et al., 2012. Fiji: an open-source platform for biological-image analysis. Nat. methods 9 (7), 676 682.

Schlüter, S., Sheppard, A., Brown, K., Wildenschild, D., 2014. Image processing of multiphase images obtained via x-ray microtomography: a review. Water Resour. Res. 50 (4), 3615 3639.

Silin, D., Patzek, T., 2006. Pore space morphology analysis using maximal inscribed spheres. Phys. A Stat. Mech. Appl. ISSN: 0378-4371 371 (2), 336–360. http://dx.doi.org/10.1016/j.physa.2006.04.048.

Sok, R.M., Varslot, T., Ghous, A., Latham, S., Sheppard, A.P., Knackstedt, M.A., 2009. Pore scale characterization of carbonates at multiple scales: integration of micro-ct, bsem, and fibsem. In: International Symposium of the Society of Core Analysts. Noordwijk, 27 30 Sept.

U.S. Energy Information Administration, 2015. Annual Energy Outlook.

Wang, L., Torres, A., Xiang, L., Fei, X., Naido, A., Wu, W., 2015. A technical review on shale gas production and unconventional reservoirs modeling. Nat. Resour. 6, 141–151. http://dx.doi.org/10.4236/nr.2015.63013.

Wang, Z., Bovik, A.C., 2002. A universal image quality index. Signal Process. Lett. IEEE 9 (3), 81–84.

Weller, H.G., Tabor, G., Jasak, H., Fureby, C., 1998. A tensorial approach to CFD using object orientated techniques. Comput. Phys. 12 (6), 620.